Cationic disorder: Governing the spin-insulatronic properties of nanocrystalline ZnFe_2O_4 thin films

Murtaza Bohra, Rémi Arras, Vidyadhar Singh, Nitesh Singh, Anil Annadi,
Evropi Toulkeridou, Panagiotis Grammatikopoulos, Hsiung Chou

To cite this version:

Murtaza Bohra, Rémi Arras, Vidyadhar Singh, Nitesh Singh, Anil Annadi, et al.. Cationic disorder: Governing the spin-insulatronic properties of nanocrystalline ZnFe_2O_4 thin films. Materials Today Communications, 2024, 38, pp.108333. 10.1016/j.mtcomm.2024.108333 . hal-04668991

HAL Id: hal-04668991
https://hal.science/hal-04668991v1

Submitted on 7 Aug 2024

Cationic disorder: Governing the spin-insulatronic properties of nanocrystalline $ZnFe_2O_4$ thin films

Murtaza Bohra [a,*], Rémi Arras [b], Vidyadhar Singh [c], Nitesh Singh [a], Anil Annadi [a], Evropi Toulkeridou [d], Panagiotis Grammatikopoulos [e,f], Hsiung Chou [g,*]

[a] *Mahindra University, Survey Number 62/1A, Bahadurpally Jeedimetla, Hyderabad 500043, Telangana, India*
[b] *CEMES, Université de Toulouse, CNRS, 29 Rue Jeanne Marvig, F-31055 Toulouse, France*
[c] *Department of Physics, Jai Prakash University, Chapra 841301 Bihar, India*
[d] *Guangdong Technion – Israel Institute of Technology, Shantou, Guangdong 515063, China*
[e] *Materials Sciences and Engineering, Guangdong Technion – Israel Institute of Technology, Shantou, Guangdong 515063, China*
[f] *Guangdong Provincial Key Laboratory of Materials and Technologies for Energy Conversion, Guangdong Technion – Israel Institute of Technology, Shantou, Guangdong 515063, China*
[g] *Department of Physics, National Sun Yat-sen University, Kaohsiung City 801, Taiwan*

ARTICLE INFO

Keywords:
Cation disorder
Curie temperature
Spin glass transition
Nanophase diagram

ABSTRACT

Controlling cation order/disorder in spinel offers a highly effective means of tailoring material properties by modifying inter- and intra-sub-lattice ionic interactions. In this study, we conducted high-temperature magnetization measurements (300–1000 K) to determine average Curie temperatures (T_C) for nanocrystalline $ZnFe_2O_4$ thin films. Thermodynamical stability of these films under extreme conditions was investigated by assessing lattice structures, oxygen vacancies, magnetization, and electric resistivity for spin-insulatronic applications. Reversible cation inversion via heat treatments (in-situ and ex-situ) yields tunable ferrimagnetic (FiM) order in $ZnFe_2O_4$, with T_C ranging from 425 to 710 K. First-principles calculations highlight effective cation inversion mitigating magnetic frustration, promoting collinear FiM ordering, and elevating T_C. Oxygen vacancies further reinforce ferrimagnetism, slightly reducing resistivity through the formation of Fe-3d gap states near the Fermi level. A proposed magnetic nanophase diagram elucidates dominant competing magnetic ground states (cluster spin-glassy state, FiM, and antiferromagnetic) with increasing growth temperature, fostering innovative homo-architectures from multiple $ZnFe_2O_4$ thin films with diverse functionalities.

1. Introduction

Generation and detection of spin current is crucial for spintronic-based information transfer and processing for future low-power "green" electronics [1]. Pure spin current stems from forcing electrons with different spins to flow in opposite directions, which can be achieved via spin pumping (SP) or the spin Seebeck effect (SSE) among other methods [2,3]. Magnetic insulators are frontrunners [3] in producing pure spin currents via magnonics in both SP and SSE processes due to their low eddy current losses and negligible anomalous Nernst effects. Epitaxial $Ni_{0.65}Zn_{0.35}Al_{0.8}Fe_{1.2}O_4$, $MgAl_{0.5}Fe_{1.5}O_4$, $Li_{0.34}Mn_{0.1}Zn_{0.32}Fe_{2.19}O_4$ and $Li_{0.5}Fe_{2.5}O_4$ spinel thin films with low damping ($\sim 10^{-3}$) have been recently explored [2,4–6] as alternatives to garnet thin films. However, the former thin films require multicomponent targets, single-crystal substrates, and high growth temperatures, making them still expensive for integration with existing spintronic technology.

Affordable and low-temperature-processed Zn-ferrite ($ZnFe_2O_4$) thin films can be ideal candidates for the aforementioned applications due to the presence of only trivalent iron (Fe^{3+}) magnetic ions, providing tunable magnetic and insulating properties with minimal microwave losses [7,8]. However, $Zn_xFe_{3-x}O_4$ and/or $ZnFeO_{4-\delta}$ thin films, when deposited in low oxygen pressures/vacuum [9–11], have exhibited resistivity values five orders of magnitude lower ($\rho_{300\ K} = 0.05 - 5 \times 10^{-3}$ $\Omega - $cm) than bulk $ZnFe_2O_4$, while also displaying high magnetizations ($4\pi M_S = 5.6$ kG) and Curie temperatures ($T_C \geq 700$ K). Therefore, simultaneous control of the electronic and magnetic properties of Zn-ferrite thin films continues to be a significant challenge. This

---

* Corresponding authors.
E-mail addresses: murtaza.bohra@mahindrauniversity.edu.in (M. Bohra), hchou@mail.nsysu.edu.tw (H. Chou).

necessitates the engineering of nanocrystalline Zn-ferrite thin films through cation inversion in an oxygen-rich environment [7,8]. Previously, we have demonstrated the ability to control a wide range of magnetic properties (superparamagnetic (SPM), ferrimagnetic (FiM), and paramagnetic (PM)) in nanocrystalline Zn-ferrite thin films depending on substrate temperature (T_S) [12]. The FiM phase shows an initial increase in $4\pi M_S$ values with T_S, which reach a maximum (3 kG) [7] and then decrease to PM bulk $ZnFe_2O_4$ values [13], attributed to reversible cation inversion. These FiM films also exhibit a low microwave linewidth (40–200 Oe) [8], paving the way for spin-insulatronics.

Here, built on prior work on Zn-ferrite thin films [7,8,12], we performed high-temperature magnetization measurements (300–1000 K) to investigate average T_C values and gain insights into cation inversion, grain size, and spin-insulatronic properties. Density functional theory (DFT) revealed the suppression of geometrical magnetic frustration and formation of defect states near Fermi levels, leading to high-temperature FiM order and slightly reduced resistivity. A detailed magnetic nanophase diagram was constructed, unveiling diverse magnetic ground states.

2. Methods

Nanocrystalline Zn-ferrite thin films with a thickness of 200 nm were laser ablated in a pure oxygen atmosphere ($P(O_2) = 0.16$ mbar) on amorphous fused quartz substrates [7]. These thin films were grown at different T_S, ranging from room temperature (RT) to 850 °C (1123 K). The crystalline structure and chemical composition were analyzed using X-ray based techniques, including X-ray diffraction (XRD) performed on a Rigaku SmartLab X-ray diffractometer with a Cu K_α X-ray source, and X-ray photoelectron spectroscopy (XPS) conducted on a Kratos AXIS Ultra DLD Photoelectron spectrometer with an Al K_α anode. The phase purity of each thin film was determined by micro Raman spectra in the range of $100 - 1000\ \text{cm}^{-1}$. Grain size distribution was determined by analyzing bright-field micrographs obtained from transmission electron microscopy (TEM) using a Philips CM 200 microscope and analyzed using ImageJ 1.46 analysis software. Magnetic properties were measured using a vibrating sample magnetometer (VSM) in an in-plane layer configuration, connected to a physical property measurement system (PPMS), where the sample was kept under a vacuum of 10^{-5} mbar within the temperature range of up to 1000 K. The high-temperature magnetization measurement (HTMM) process is equivalent to vacuum annealing and includes in-situ measurements. Two measurement cycles were applied to the samples. Cycle-I measured temperatures from 300 to 800 K and then returned to 300 K, with a ramp rate of 12 K/min and a fixed field of 5 kOe. Cycle-II covered the temperature range from 300 K to 1000 K without removing the sample of Cycle-I from the chamber, using the same ramp rate and applied field. Afterward, the sample was cooled to 5 K, and a low-temperature magnetization measurement (LTMM) was conducted while maintaining a constant flow of helium gas between 5 and 300 K, along with the same ramp rate and applied field. The diamagnetic contribution of the quartz substrate and sample holder was subtracted from the magnetization data.

DFT calculations were performed using the Vienna *Ab initio* Simulation Package (VASP) [14,15] and the projector augmented-wave (PAW) method [16], with a cut-off energy of 600 eV. We used the exchange-correlation energy functional parametrized by Perdew, Burke, and Ernzerhof (PBE) [17] with a "$+U$"-dependent correction [18] added to the *3d* bands of Fe atoms and a U_{eff} parameter of 4.5 eV. The first Brillouin zone associated to the conventional spinel cubic cell was sampled with a Monkhorst-Pack grid [19] of $6 \times 6 \times 6$ $\boldsymbol{k}$-vectors. The spinel structure is formed by a distorted face-centered lattice of oxygen atoms. When the structure is stoichiometric and adopts a normal cation distribution, the divalent Zn^{2+} cations are located in tetrahedral atomic sites (A), while all trivalent Fe^{3+} cations occupy octahedral sites (B). The presence of cation disorder is mostly attributed to Zn^{2+}/Fe^{3+} cation exchanges between A and B sites, according to the chemical formula $\left[Zn^{2+}_{1-x}, Fe^{3+}_{x}\right]_A\left[Zn^{2+}_{x}, Fe^{3+}_{2-x}\right]_B O^{2-}_4$, where x is called the inversion degree. When the spinel structure is perfectly inverse, the most stable Zn^{2+}/Fe^{3+} cation ordering in B sites corresponds to the space group $P4_122$ (No. 91). Structures with an intermediate inversion degree were generated by keeping this cation distribution in B sites fixed [20]. For every structure, different magnetic configurations (FM, AFM, or FiM) were tested. The Heisenberg exchange integrals J_{ij} were calculated using the Liechtenstein-Katsnelson-Antropov-Gubanov formula [21] implemented in the QuantumATK code [22,23]. With this method, all the exchange integrals between a specific atom and the neighboring atoms included in a range of 3 conventional cells (i.e., with a maximum nearest-neighbor distance of ≈ 20 Å) were calculated. These integrals were then used to obtain the Curie Temperature T_C^{MFA} within the mean-field approximation (MFA) [24].

3. Results and discussion

In the present study, three sets of nanocrystalline Zn-ferrite thin films, namely *ZFRT* (T_S of RT), *ZF350* (T_S of 350 °C), and *ZF850* (T_S of 850 °C), were selected for detailed magnetization studies. These films exhibit single-phase $ZnFe_2O_4$ (Supplementary Material Fig. S1) with three types of grain size distributions (Supplementary Material Fig. S2). The average grain sizes (estimated from TEM micrograph and Scherrer formula), lattice constants (estimated from Rietveld analysis), and magnetic transition temperatures [12] are presented in Table 1. The *ZFRT* layer predominantly contained small-sized grains (10–20 nm) and exhibited a dominant SPM behavior at 300 K, with a blocking temperature (T_B) of 100 K. In contrast, the *ZF350* layer, composed mainly of intermediate-sized grains (25–35 nm), showed a dominant FiM order. Finally, the *ZF850* layer, with larger grain sizes (50–70 nm), displayed a dominant bulk $ZnFe_2O_4$ PM behavior with Néel temperature T_N of 15 K.

The $M-T$ curves for the *ZFRT*, *ZF350*, and *ZF850* thin films under HTMM ($305\ \text{K} \le T \le 1000\ \text{K}$) at a fixed field of 5 kOe are shown in Fig. 1(a-d) for both heating and cooling cycles. No impurity phases (Supplementary Material Fig. S1) were detected after HTMM; only grain growth and slight increment in lattice parameters (Table 1). Distinct $M-T$ behaviors can be observed in all three thin films. Susceptibility (χ) vs. T curves of *ZF850* thin films follow Curie-Weiss law, $C/T\text{-}\theta$ of PM behavior, during reversible heating–cooling cycles (Fig. 1(a)) with slight presence of ferromagnetic interactions below Weiss temperature θ=226 K. This feature is expected because the maximum temperature of HTMM (800 K) is not higher than T_S, resulting in no discernible change in the crystalline structure in Cycle-I (Supplementary Material Fig. S1),

Table 1
Spontaneous magnetization ($4\pi M_S$), magnetic ordering temperatures (average Curie temperature $\overline{T_C}$, Néel temperature T_N, and blocking temperature T_B), lattice constants, average grain size [7]and resistivity ($\rho_{300\ K}$) measured at 300 K for Zn-ferrite thin films at different T_S before and after HTMM.

As-grown thin films	*$4\pi M_S$ (kG)*	*Lattice constant (Å)*	*Transition temperature (K)*	*Grain sizes (nm)*	*Resistivity $\rho_{300\ K}$ (Ω-cm)*
ZFRT	0.4	-	$T_B = 100$	14	$> 10^4$
ZF350	3	8.416	$\overline{T_C} = \sim 589$	31	2.5×10^2
ZF850	0.2	8.446	$T_N = 15$	68	$> 10^4$
Bulk	0.02	8.44	$T_N = 15$	-	2×10^2
After HTMM					
ZFRT (Cycle-I)	2.1	8.433	$\overline{T_C} = \sim 710$	46	1.3×10^1
ZF350 (Cycle-I)	3.3	8.418	$\overline{T_C} = \sim 557$	46	3.1×10^1
ZF350 (Cycle-II)	1.3	8.421	$\overline{T_C} = \sim 425$	56	2.1

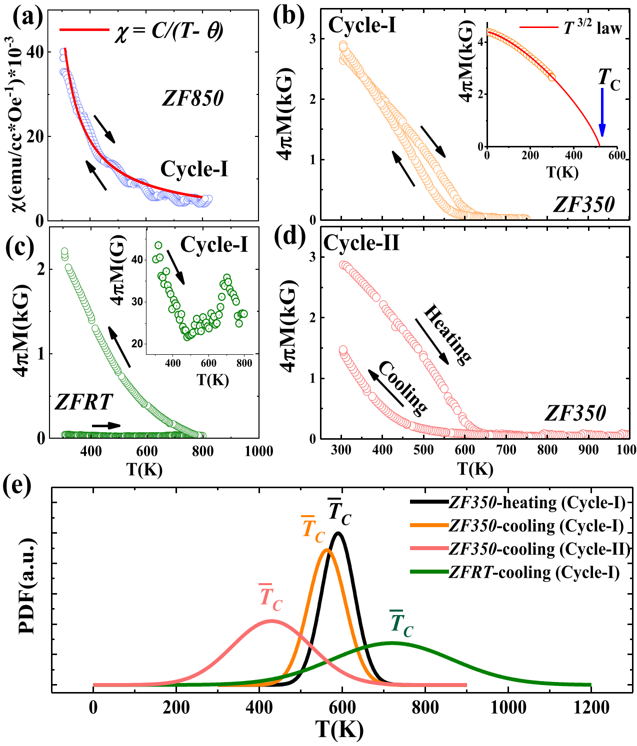

Fig. 1. χ vs.T curves of ZF850 layer (a), M−T curves of ZF350 layer (b-d), and ZFRT (c) during HTMM heating and cooling cycle measured at 5 kOe. In Cycle-I, the ZF350 layer was heated up to 800 K, and in Cycle-II it was heated up to 1000 K. The inset (b) shows the M−T curve at 5 kOe in LTMM (5 − 300 K) (green open circle) and the fitted curve (red solid line) using Bloch $T^{3/2}$ law. The inset (c) shows a larger view of the heating cycle M−T curve of ZFRT. The T_C probability distribution functions were obtained from fitted M−T curves in equation-1(e).

so we will not discuss it further.

A notable disparity in the $M-T$ behavior can be observed between the heating and cooling stages of the *ZFRT* thin films (Fig. 1(c)). During the heating process up to a maximum temperature of ~800 K ($> T_S$), the thin films initially exhibit PM behavior with a decrease in magnetization. However, at around 700 K, a peak develops (inset of Fig. 1(c)). In the cooling stage, the magnetization increases with decreasing temperature, until reaching 305 K. This behavior suggests the crystallization of amorphous/disordered $ZnFe_2O_4$ phases during the heating stage Cycle-I (Supplementary Material Fig. S1), leading to FiM behavior. Interestingly, during the heating of ZF350 thin films in Cycle-I (Fig. 1(b)), a gradual decrease in magnetization is observed over a broad temperature range, and magnetization vanishes at around 650 K, indicating progressive grain growth during the heating stage (Table 1). While in the cooling stage, the $M-T$ curve lies above that of the heating stage, with slight hysteresis, suggesting that heating up to 750 K ($> T_S$) causes grain growth. This conclusion is further supported by the extrapolated T_C values of 550 K obtained from Bloch $T^{3/2}$ law fitting of the low-temperature $M-T$ curve (inset of Fig. 1(b)), assuming a fixed composition and grain sizes. This FiM behavior can be attributed to a cation inversion [25], with the displacement of some of Fe^{3+} ions from the octahedral sites to the tetrahedral sites. Notably, the magnetization curve of ZF350 thin films (Cycle-II) (Fig. 1(d)) during the cooling stage is lower than those of the heating stage, with magnetization vanishing around 500 K. This indicates that further heating up to 1000 K ($> T_S$) leads to larger grain sizes approaching the bulk's paramagnetic structure (Table 1). Thus, high-temperature treatments, no matter whether during high-temperature growth or during HTMM, lead to grain growth and distributions of grain sizes. Moreover, the HTMM process was conducted in vacuum, so the presence of oxygen vacancies and the transformation of a few Fe^{3+} (5 μ_B) ions into Fe^{2+} (4 μ_B) ions at this stage cannot be ruled out, which may lead to lower electric resistivity values (Table 1) compared with the bulk $ZnFe_2O_4$. The average magnetization in a heterogeneous FiM granular system can be expressed by assuming a Gaussian distribution function for the sample-specific T_C values based on the Central Limit Theorem [26,27] as:

$$< M(T) >= \int_0^\infty M_0\left(\frac{T_c - T}{T_c}\right)^\beta \quad \theta(T_C - T)\frac{1}{\sqrt{2\pi}\Delta T_c}e^{\frac{-(T_c-\overline{T_c})^2}{2\Delta T_c^2}} \quad dT_c \tag{1}$$

Here, $\overline{T_C}$ represents the average Curie temperature and ΔT_C is the width of the Curie temperature distribution. M_0 is the saturation magnetization, β is the critical exponent (1.2 −1.5), and θ is the Heaviside function, ensuring that $M(T)$ equals zero for $T > T_C$. The experimental $M-T$ curves were fitted near T_C using the least-squares method (Supplementary Material Fig. S3). The $\overline{T_C}$ values of our nanocrystalline Zn-ferrite thin films are given in Table 1. The as-grown *ZF350* layer shows $\overline{T_C} = \sim 589$ K, which is reduced after HTMM to 557 K and 425 K in Cycle-I and Cycle-II, respectively. The drift of $\overline{T_C}$ values of the *ZF350* thin films toward lower temperatures is more clearly demonstrated in their probability distribution functions (PDFs), as shown in Fig. 1(e), after Cycle-I and II. The higher ΔT_C in Cycle-II (95 K) compared to Cycle-I (45 K) can be attributed to the larger differences in nanograin size distribution within the thin films. After HTMM, *ZFRT* thin films transform into FiM with an increased $\overline{T_C} = \sim 710$ K, along with a distribution width $\Delta T_C = 150$ K. These thin films show large $\overline{T_C}$ values with $4\pi M_S$ values (2.1 kG). In Cycle-I of *ZF350* thin films, $\overline{T_C}$ is lower (~557 K) but show higher $4\pi M_S$ values (3.3 kG), indicating different inter- and intra-sublattice magnetic couplings.

Room temperature Raman spectra were obtained to investigate cation disorder in Zn-ferrite thin films before and after HTMM, as shown in Fig. 2(a-b). The bulk $ZnFe_2O_4$ Raman data are also included in Fig. 2

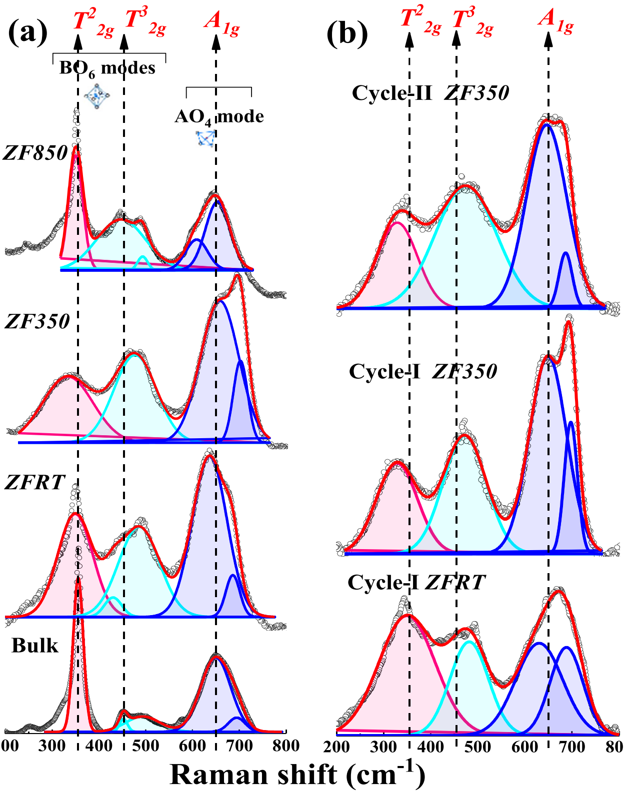

Fig. 2. Raman spectra of ZFRT, ZF350 and ZF850 thin films along with deconvoluted Raman data using Lorentzian peak functions before (a) and after HTMM (b).

(a) for comparative study. We observed fewer Raman modes (A_{1g}, T_{2g}^{2} and T_{2g}^{3}) than the theoretically predicted five modes (A_{1g}, E_g and three T_{2g}), but no extra peaks from impurity phases were detected [28]. In spinel ferrites, the A_{1g} modes above 600 cm^{-1} correspond to the motion of oxygen atoms in tetrahedral AO_4 sites, while the low-frequency modes are associated with vibrations within the octahedral BO_6 sites. The Raman spectra were fitted with five distinct peaks using Lorentzian functions. The peak positions of the A_{1g} and T_{2g}^{2} modes in the as-grown Zn-ferrite thin films (Fig. 2(a)) exhibited a significant red shift, indicating a shift towards smaller wavenumbers compared to the bulk data. In *ZFRT* and *ZF350* thin films, the peak at 352 cm^{-1} (T_{2g}^{2}) broadens, and the peak at 447 cm^{-1} (T_{2g}^{3}) shows a broad shoulder at higher wavenumbers. In ZF850 thin films, however, these two peaks closely resemble bulk spectra. This observation suggests that smaller grain sizes cause cation disorder [28]. The broad peak at 650 cm^{-1} (A_{1g}) observed in Zn-ferrite thin films can be separated into two Lorentzian peaks, ranging between around $610-650$ cm^{-1} and $685-698$ cm^{-1}. The former Raman modes can be attributed to oxygen breathing vibrations against Zn^{2+}, while the latter modes are associated with oxygen vibrations against Fe^{3+}. This suggests the coexistence of ZnO_4 and FeO_4 groups. If the vibrational frequencies of the two modes were very close, only a single broad peak would be observed. Otherwise, vibrations related to different cations at the same site may exhibit two distinct first-order Raman modes. In *ZFRT* and *ZF350* thin films, the increased intensity ratio of the FeO_4 vibration compared with the ZnO_4 vibration suggests the incorporation of more Fe ions into the tetrahedral A sites. This rearrangement of cations results in the formation of two magnetic sublattices, which contribute to the enhanced magnetization compared to bulk $ZnFe_2O_4$. Similarly, the A_{1g} peak (650 cm^{-1}) in *ZF850* thin films is located at a similar position as in bulk $ZnFe_2O_4$, with a shoulder around 610 cm^{-1}. Comparing the Raman spectra measured after HTMM, we observe further broadening of the T_{2g}^{2} and T_{2g}^{3} peaks, as depicted in Fig. 2(b). In *ZFRT* and *ZF350* thin films heated at $750-800$ K (Cycle-I), the T_{2g}^{2} peaks exhibit a noticeable red-shift, and the intensity of the shoulder of the T_{2g}^{3} peak at higher wavenumbers increases, directly resulting from the replacement of Fe atoms by heavier Zn atoms at the octahedral BO_6 sites. The intensity ratio of the FeO_4 vibration to the ZnO_4 vibration, associated with the A_{1g} peaks, changes from 1:1 to 3:1 in *ZFRT* and *ZF350* thin films, indicating an increase in cation inversion. However, this ratio is reduced in *ZF350* thin films upon further heating at 1000 K (Cycle-II), as the cation distribution starts to revert back to the normal bulk structures, which is supported by XRD and magnetic studies. The ratio between the two T_{2g}^{2} and A_{1g} Raman scattering peaks appears to depend on the degree of inversion; the former signal is dominant in normal structure, while the latter is dominant in inverted structure.

We observed that cation disorder can lead to significant changes in symmetrical vibrations. Furthermore, heating under vacuum can introduce structural defects, such as oxygen vacancies, which can alter the local electronic properties and influence the electron-phonon interaction in Zn-ferrite thin films. Allen's formula [29] was utilized to estimate the strength of electron-phonon coupling (λ_i) associated with the decay of phonons into electron-hole pair excitations and the resulting additional broadening. This estimation was based on the observed line shape parameters, including the peak position (ω) and the full width at half maximum (Γ_i). The relationship is given by:

$$\lambda_i = \frac{\Gamma_i}{\omega^2}\left[\frac{g_i}{2\pi N(E_F)}\right] \tag{3}$$

where g_i represents the degeneracy of the i^{th} mode and $N(E_F)$ is the density of states at the Fermi level. Though the precise values of λ_i cannot be estimated, we have presented the relative variations in λ_i values for the high-intensity A_{1g} and T_{2g}^{2} modes in Table 2. We also include the data for bulk $ZnFe_2O_4$, using a theoretical $N(E_F)$ (3 states eV^{-1} f.u.$^{-1}$) at 300 K. The enhanced λ_i values observed in the as-grown *ZFRT* (A_{1g}–0.09, T_{2g}^{2}–0.88) and *ZF*350 (A_{1g}–0.14, T_{2g}^{2}–1.38) thin films compared to bulk $ZnFe_2O_4$ (A_{1g}–0.05, T_{2g}^{2}–0.13) and *ZF*850 layer (A_{1g}–0.06, T_{2g}^{2}–0.74) suggest an increase in spin disorder resulting from the redistribution of cations between the interstitial A and B sites and the formation of an inverse spinel structure [30]. The spin disorder in the *ZFRT* (A_{1g}–0.16, T_{2g}^{2}–1.07) and ZF350 (A_{1g}–0.17, T_{2g}^{2}–1.58) thin films increases after Cycle-I of HTMM. The changes in the T_{2g}^{2} mode result from the symmetric and asymmetric bending of Fe-O bonds at the octahedral B sites, which affect both the electronic and structural properties [30,31]. Consequently, the highest λ_i values can be attributed to the electronic disorder arising from defects/oxygen vacancies and the partial transformation of Fe^{3+} ions into Fe^{2+} at the B sites. However, if this had been the sole cause, the λ_i values would have continued to increase after Cycle-II of HTMM. The observed trend (A_{1g}–0.11, T_{2g}^{2}–1.13) suggests that cation disorder plays a dominant role over the electronic disorder and that it is reduced after Cycle-II, thus approaching the cation distribution of the normal spinel structure.

Table 2

Line shape parameters; peak position (ω) and full width at half maximum (Γ_i) and electron-phonon coupling strength (λ_i) for A_{1g} and T_{2g}^{2} Raman modes for Zn-ferrite thin films before and after HTMM.

As-grown thin films	T_{2g}^{2} mode			A_{1g} mode		
	Γ (cm^{-1})	ω (cm^{-1})	λ	Γ (cm^{-1})	ω (cm^{-1})	λ
ZFRT	83.1	347.7	0.88	96.7	658	0.09
ZF350	121.8	329.9	1.38	126.3	656	0.14
ZF850	70.5	347.3	0.74	80.9	647	0.06
Bulk	-	-	0.13	-	-	0.05
After HTMM						
ZFRT (Cycle-I)	99.6	336.9	1.07	169.5	669.5	0.16
ZF350 (Cycle-I)	134.01	335.9	1.58	180.4	664	0.17
ZF350 (Cycle-II)	94.1	326.9	1.13	108.7	654.5	0.11

XPS analysis further confirms the cation inversion and the presence of only Zn^{2+} and Fe^{3+} ions in as-grown Zn-ferrite thin films (Supplementary Material Fig. S4). The influence of HTMM in Cycle-I and II on the surface chemical composition and ionic state of *ZFRT* and *ZF350* thin films are investigated in Fig. 3(a-b). The Fe *2p* XPS spectra exhibit two peaks, Fe $2p_{3/2}$ (~711.4 eV) and Fe $2p_{1/2}$ (~725 eV), of $ZnFe_2O_4$ without any iron oxides (FeO, $\alpha/\gamma-Fe_2O_3$ and Fe_3O_4) impurity phases [32–34]. The satellite peak at binding energies (BE) = 718–719 eV indicates the dominance of Fe^{3+} ions [32–34]. Fe^{2+} ions, which have a satellite peak at 714–715 eV and an Fe $2p_{3/2}$ peak around 709.5 eV, are absent [35]. The asymmetric Fe $2p_{3/2}$ peaks suggest that the inversion parameters are greater than zero. Specifically, the Fe^{3+} ions occupying tetrahedral sites exhibit higher BE for their *2p* electrons compared to Fe^{3+} ions occupying octahedral sites. This is because tetrahedral coordination involves fewer O^{2-} anions, resulting in lower electron density within their coordination sphere [36]. The higher BE peaks observed in the as-grown *ZFRT* thin films may indicate incomplete ferrite formation [34], which is supported by the XRD results. However, after HTMM Cycle-I, the width of the Fe $2p_{3/2}$ peak narrowed down, although it remained broader than that of bulk $ZnFe_2O_4$. Conversely, the Fe *2p* peaks of *ZF350* layer after HTMM Cycle-II approached the BE values of the bulk, and their intensity was significantly low.

In the insets of Fig. 3(a-b), we also plot the O-*1 s* edge spectra of both thin films before and after HTMM. These asymmetric curves of O-*1 s* can be divided into two peaks around 529.5 eV and 531.8 eV, indicating different oxygen environments [37–40]. The peak, centered around 529.5 eV, corresponds to lattice oxygen ions (O_L), while the higher binding energy peak at 531.8 eV is attributed to oxygen vacancies (O_V). After Cycle-I and Cycle-II, the LTMM *M-T* curves (5- 300 K) of the Zn-ferrite thin films plotted in Fig. 3(c-d) do not exhibit a Verwey transition, which is typically associated with the presence of both Fe^{3+} and Fe^{2+} ions at octahedral sites of Fe_3O_4, confirming the absence of the

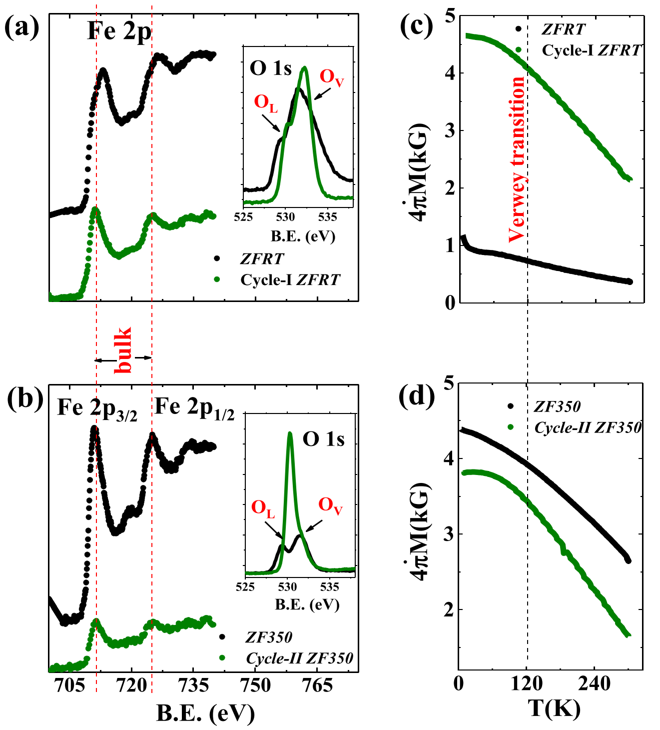

Fig. 3. XPS spectra of Fe_{2p} before and after HTMM for ZFRT(a) and ZF350 (b) thin films. Insets show their $O_{1\,s}$ spectra. Corresponding LTMM, M− T curves (5 − 300 K) for ZFRT (c) and ZF350 thin films(d) at 5 kOe before and after HTMM.

Fe^{+2} ions in our Zn-ferrite thin films. In the literature, Zn-ferrite thin films grown with very low oxygen content [10] resulted in the formation of mixed Fe^{2+}/Fe^{3+} valence phases $[Zn_x^{2+}Fe_{1-x}^{3+}]_A[Fe_{1+x}^{3+}Fe_{1-x}^{2+}]_BO_4$, or even of binary oxides (Fe-O and Zn-O) during annealing at high temperature, which seriously jeopardizes the stability of the Zn-ferrite thin films [41,42]. Thus, the present results are significant because our Zn-ferrite thin films only lose their unique magnetic and electric properties at elevated temperatures beyond the requirements of SP and SSE applications (≥ 800 K). As confirmed by our DFT calculations, discussed in the later section, defect gap states can be induced by the presence of oxygen vacancies, which may affect aforesaid properties.

The cation distribution and degree of inversion x are influenced by the growth and HTMM conditions, which may modify the content of oxygen vacancies δ [42,43]. To understand how these two parameters, affect the electronic and magnetic properties, we performed DFT simulations. Table 3 summarizes the variations of lattice parameters, spin-resolved band gaps, and magnetic couplings as a function of the inversion degree x.

First, let us consider the case of the stoichiometric spinel $ZnFe_2O_4$ ($\delta = 0$) with a normal cation distribution ($x = 0.0$), where all Fe^{3+} ions occupy the octahedral B sites. As Zn^{2+} cations are in a $3d^{10}$ electronic configuration, they display no magnetic moment, and the magnetic interactions thus remain confined within the octahedra ($J_{AA} = J_{AB} = 0$) through their connection via edge-sharing O_{2p} orbitals. This leads to weak AFM superexchange couplings ($J_{BB} < 0$) with nearly-90° o $Fe_B^{3+} - O - Fe_B^{3+}$ bridges, as schematically shown in Fig. 4(a). We calculated that the J_{BB} constants display low values, with a similar order of magnitude varying between -0.60 and -1.49 k_BK, for interactions between the 1st- to 4th-neighbor atoms (see Supplementary Material Table S1, which also provides a comparison with the J values calculated by Quintero *et al.* [44]), before falling to nearly 0 k_BK. All these interactions having the same sign means that the system undergoes magnetic frustrations and that we can, in consequence, expect that the magnetic ground state of $ZnFe_2O_4$ could correspond to a non-collinear magnetic ordering. Using these values, we calculated an order temperature $T_N = 14.8$ K, which matches our experimental measurements. By mapping several collinear orderings, we found that the more stable magnetic configuration corresponds to the antiferromagnetic ordering ($M_S = 0$ μ_B) that lowers the symmetries of the system to that of the space group $P4_122$ and in which the antiferromagnetic coupling is set between pairs of ferromagnetically-coupled first-neighbor Fe atoms; this result agrees with the calculations reported by Quintero *et al.* [45].

In the event of cation inversion (x ‡ 0), even at a very low inversion degree such as $x = 0.125$, there is a significant alteration in magnetic ordering due to the presence of Fe^{3+} and Zn^{2+} cations in the A and B sites, respectively. As x varies from 0.125 to 1.0, the number of $Fe_A^{3+} - O - Fe_B^{3+}$ couplings increase, with a bond angle of nearly 125° and extremely-negative J_{AB} values. This confirms the expected remarkably strong AFM couplings between A-B sites [46]; approximately 20 times higher than the initial J_{BB} calculated for $x = 0$. This also results in a change of the J_{BB} parameters to positive values, signifying ferromagnetic couplings within the B sublattice, as schematically shown in Fig. 4(b).

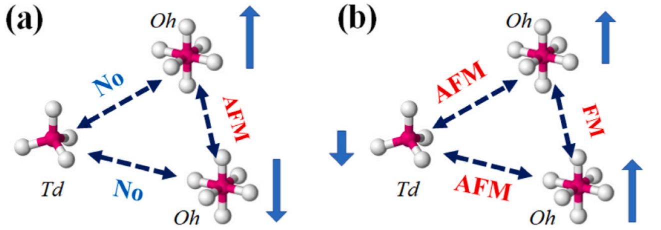

Fig. 4. (a) Schematic of spin structure of the pure $ZnFe_2O_4$, where the magnetic Fe^{3+} cations inhabit the center of the octahedron, Oh, and couple antiferromagnetically ($J_{BB} < 0$). (b) Schematic spin structure of $(Zn_{1-x}Fe_x)(Zn_xFe_{2-x})O_4$, for a degree of inversion. In this structure, the Fe^{3+} cations can be located in the tetrahedron sites, Td, that strongly couple antiferromagnetically with the Fe^{3+} ions at Oh sites ($J_{AB} < 0$), thus forcing the Fe^{3+} ions in Oh sites to be coupled ferromagnetically ($J_{BB} > 0$).

Table 3

Calculated variations of pseudo-cubic lattice parameter a, band gap at the Fermi level, E_g, and total spin magnetic moment, M_S, as a function of the inversion degree, x. The more stable magnetic ordering calculated with the QuantumATK code is also given, with the corresponding exchange integrals, J_{AB} and J_{BB}, between first-neighbor Fe atoms and the resulting Curie temperature, T_C^{MFA}, calculated within the MFA.

x	*a* (Å)	*E_g* (eV)		*Mag. config.*	M_s (μ_B/f.u.)	J_{AB}/k_b (K)	J_{BB}/k_b (K)	T_C^{MFA} (K)
		Maj. spin	Min. spin					
0.0	8.518	1.88	1.88	$[\uparrow_{8/8},\downarrow_{8/8}]_B$	0.0	-	-0.60	14.8
0.125	8.518	1.78	1.74	$(\downarrow_{1/8})_A[\uparrow_{15/8}]_B$	8.75	-26.31	0.73	273.7
0.25	8.515	2.03	1.55	$(\downarrow_{2/8})_A[\uparrow_{14/8}]_B$	7.5	-24.27	8.57	351.3
0.5	8.507	1.88	1.55	$(\downarrow_{4/8})_A[\uparrow_{12/8}]_B$	5.0	-20.56	9.72	506.7
0.75	8.496	1.96	1.63	$(\downarrow_{6/8})_A[\uparrow_{10/8}]_B$	2.5	-22.67	8.73	530.5
1.0	8.487	1.98	2.17	$(\downarrow_{8/8})_A[\uparrow_{8/8}]_B$	0.0	-21.29	8.38	558.2

The ferromagnetic coupling in B-B chains is believed to be due to the dominant AFM coupling within A-B sites [41,47], which overrides the inherent AFM coupling along B-B chains. This transformation leads to the establishment of FiM ordering, accompanied by an increase in both the net M_S and T_C. The calculated maximum of the net magnetization, 8.75 μ_B, is obtained for the lowest value of $x = 0.125$. It is then followed by a gradual decrease of M_S when x increases, because of the higher number of Fe^{3+} cations in A site, which have spin magnetic moments antiparallel to that of Fe_B^{3+}; M_S becomes zero at $x = 1.0$, when there is exactly the same amount of Fe^{3+} cations in A and B sites. In addition to the decrease of the net magnetization when $x > 0$ increases, we calculated an enhancement of T_C because of the higher number of $Fe_A^{3+}-O-Fe_B^{3+}$ bridges, which carry the dominant AFM interaction. This explains why our as-grown *ZF350* and annealed *ZFRT* and *ZF350* (Cycle-I) thin films exhibit large *Ms*.

Furthermore, with an increase in the degree of inversion, the lattice constants are found to be smaller. This phenomenon cannot be explained solely by the simple inversion effect; oxygen vacancies have to be considered. In the absence of oxygen vacancies, $ZnFe_2O_4$ exhibits an insulating behavior due to its relatively large bandgap, ranging from 1.55 to 1.98 eV (depending on x), as shown in Table 3 and represented in the densities of states (DOS) of Figs. 5(a) and 5(b).

We propose now to investigate the effect of a neutral oxygen vacancy (V_O) on the electronic and magnetic properties. To do so, we performed additional ab initio calculations considering an oxygen-deficient $ZnFe_2O_4$ crystal ($\delta = 0.125$) with a partially-inverse spinel structure ($x = 0.5$): $[Zn_{0.5},Fe_{0.5}][Zn_{0.5},Fe_{1.5}]O_{3.875}$. Depending on the position of the Vo, two scenarios are possible: the V_O can be located near a Zn_A or near a Fe_A atom in a tetrahedral site. At high temperatures, where the distribution of V_O is expected to be random, the occurrence of each scenario will mainly depend on the number of Fe atoms in A sites, represented by the inversion degree x. In the first case, when V_O is near a Zn_A atom, the two electrons will be transferred solely to octahedra and distributed among Fe_B atoms, first-neighbors of the vacancy. The corresponding DOS is shown in Fig. 5(c), where two gap states are created near the Fermi level, only in the minority-spin channel, resulting in a decrease of the total spin magnetic moment by 2 μ_B per V_O. On the other hand, in the second case, when V_O is near a Fe_A atom, one electron will reduce the oxidation state of the first-neighbor Fe_A cation, while the second electron will be distributed onto the nearest Fe_B ions [20,48] [Fig. 5(d)], leading to the formation of one gap state in each spin channel and leaving the total spin magnetic moment unchanged, if compared to the stoichiometric compound (where $ZnFe_2O_4$ with $x = 0.5$ is predicted to be FiM). In either scenario (Figs. 5(c) and 5(d)), new defect states give rise to a smaller bandgap, which may explain the lowering of the resistivities by one to two orders of magnitude measured after HTMM in the *ZFRT* and *ZF350* (Cycle-I and Cycle-II) thin films (Table 1). In their numerical study, Quintero *et al.*, moreover predicted that reduced $ZnFe_2O_4$ oxides would display higher inversion degree and that the presence of oxygen vacancies strengthens the ferrimagnetic ordering [45].

Based on experimental low- and high-temperature magnetic studies, a magnetic nanophase diagram was constructed for nanocrystalline Zn-ferrite thin films with varying T_S at fixed magnetic field of 0.5 kOe, which indicates different dominant magnetic behaviors, as shown in Fig. 6. Of course, these correspond to prevailing magnetic phases only, and do not imply full homogeneity in the samples. By increasing T_S, the Zn-ferrite thin films undergo various magnetic states, transitioning from cluster-glass (CG) to FiM and eventually reaching a PM bulk state. Consequently, different magnetic ordering temperatures (T_C, T_N, and T_G) can be obtained in Zn-ferrite thin films due to the distribution of nano-grains produced at different T_S. The growth of stoichiometric Zn-ferrite thin films through physical vapor deposition at low T_S (<500 °C) often leads to the formation of disordered $ZnFe_2O_4$. This disorder, characterized by the inversion parameter x, arises from the quenching of randomly distributed Zn^{2+} and Fe^{3+} vapor phases. It results in a strong $J_{AB}(Fe^{3+}-Fe^{3+})$ AFM interaction. However, at low

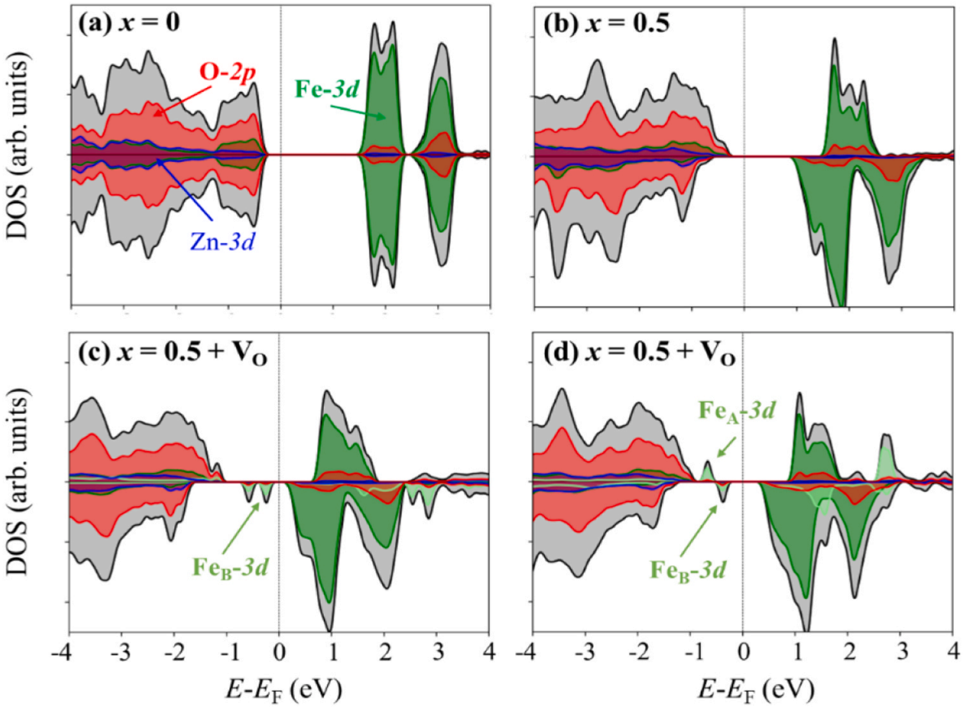

Fig. 5. Densities of states (DOS) calculated for bulk $ZnFe_2O_4$ with (a) a normal spinel structure ($x = 0$) and an AFM ordering, and (b,c,d) a partially inverse spinel structure ($x = 0.5$) and a FiM ordering. In (c) and (d), an oxygen vacancy has been introduced by removing 1/32 oxygen atoms. In (c), the tetrahedral site, first neighbor of the oxygen vacancy, is occupied by a Zn atom, while in (d) it is filled by a Fe_A atom. Atom contributions to the DOS are represented in colors; light-green DOS highlight the presence of defect states. Positive and negative DOS are for majority and minority spin projections, respectively. (For interpretation of the references to color in this figure legend, the reader is referred to the web version of this article.)

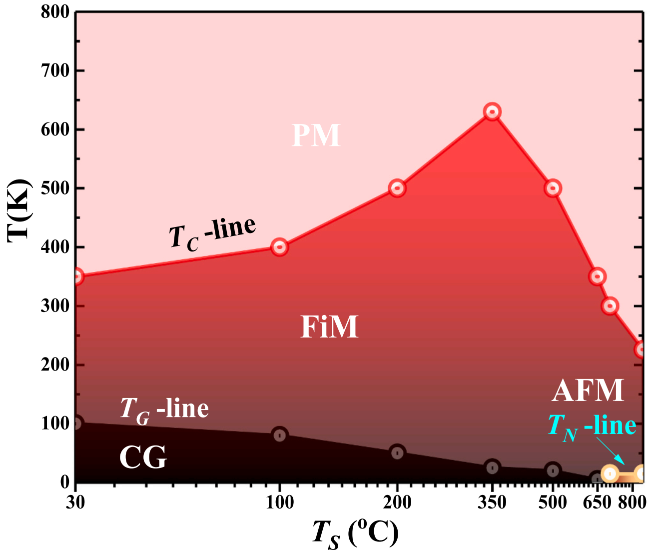

Fig. 6. Magnetic phase diagram describing various dominant magnetic phase transitions with changing T_S from RT to 850 °C at fixed magnetic field of 0.5 kOe.

temperatures these thin films exhibit CG behavior, as confirmed by the de Almeida-Thouless relationship between T_G and the applied field H [49]. In the case of low T_S = RT, the T_G value reached approximately 100 K. The origin of the dominant high-T_G CG behavior could be attributed to spin frustration in smaller grain-sized thin films, resulting from the competition between AFM interactions (Fe_A-Fe_B and Fe_B-Fe_B) within the grains, as well as the competition between AFM and FiM grains. Additionally, the presence of random oxygen deficiency may affect the overall J_{AB} and J_{BB} interactions. However, in higher T_S cases (500 – 850 °C), the cation inversion begins to revert back to its original bulk $[Zn^{2+}_{A}Fe^{3+}_{2B}O_4]$ structure, wherein the weaker J_{BB} AFM interaction dominates below $T_N = 15$ K. The T_S window (100 – 450 °C) exhibits interesting dominant FiM properties because of strong J_{AB} coupling, with higher T_C values (350 – 650 K). Thus, the constructed magnetic phase diagram may hold significant implications for integrating various Zn-ferrite thin films of different properties into lattice compatible homo-spintronic architectures such as magnetic tunnel junctions including spin-filtering barriers, exchange bias (FM/AFM) structures, opto-magnetic switches and next-generation devices based on the use of pure spin currents. However, operating temperatures of these devices should not be higher than the transition temperatures T_C, T_N, and T_G of the Zn-ferrite thin films, which, as demonstrated in this study, can be engineered by an appropriate choice of growth conditions.

4. Conclusions

The current study presents the dependence of the structural, electronic, and magnetic properties of $ZnFe_2O_4$ nanocrystalline films on their deposition temperature and subsequent thermal treatment, using a combination of experimental and theoretical methods. The most interesting findings include the spontaneous magnetization in most samples, with tunable average Curie temperatures ranging from 425 to 710 K (especially after annealing up to 1000 K), in contrast to the bulk antiferromagnetic order. X-ray photoemission spectroscopy and low-temperature magnetization measurements reveal no evidence of Fe^{2+} but indicate spinel inversion, where Fe^{3+} occupy the tetrahedral sites. Raman spectra analysis further supports the nature of cationic disorder through the weighting of vibration modes of tetrahedra FeO_4 over octahedra FeO_6. DFT calculations suggest that structural inversion and oxygen vacancies can give rise to ferrimagnetism and slightly reduced resistivity values by forming Fe-3d gap states near the Fermi level. A proposed magnetic nanophase diagram elucidates the dominant competing magnetic ground states (cluster spin-glassy state, ferrimagnetic, and antiferromagnetic) with increasing growth temperature. This exploration sets the stage for the development of innovative homo-architectures utilizing multiple $ZnFe_2O_4$ thin films with diverse spin-insulator functionalities.

Author agreement statement

We the undersigned declare that this manuscript is original, has not been published before and is not currently being considered for publication elsewhere. We confirm that the manuscript has been read and approved by all named authors and that there are no other persons who satisfied the criteria for authorship but are not listed. We further confirm that the order of authors listed in the manuscript has been approved by all of us. We understand that the Corresponding Author is the sole contact for the Editorial process. He/she is responsible for communicating with the other authors about progress, submissions of revisions and final approval of proofs.

CRediT authorship contribution statement

Bohra Murtaza: Writing – original draft, Methodology, Investigation, Formal analysis, Data curation, Conceptualization. **Arras Rémi:** Investigation, Formal analysis. **Singh Vidyadhar:** Methodology. **Singh Nitesh:** Investigation. **Annadi Anil:** Writing – review & editing. **Toulkeridou Evropi:** Methodology, Formal analysis. **Grammatikopoulos Panagiotis:** Writing – review & editing. **Chou Hsiung:** Writing – original draft, Formal analysis.

Declaration of Competing Interest

The authors declare the following financial interests/personal relationships which may be considered as potential competing interests: We do not have any conflict of interest. If there are other authors, they declare that they have no known competing financial interests or personal relationships that could have appeared to influence the work reported in this paper.

Data availability

The data that support the findings of this study are available from the corresponding author upon reasonable request.

Acknowledgements

We extend our appreciation to the Okinawa Institute of Science and Technology (OIST), Japan and IIT-Bombay, India, for generously allowing us to use their experimental facilities. This work was granted access to the HPC resources of CALMIP Supercomputing Center under the allocation. National Science Council of Taiwan grant 111-2112-M-110 -018. CORE RESEARCH GRANT - CRG/2023/002577 by SERB, India.

Appendix A. Supporting information

Supplementary data associated with this article can be found in the online version at doi:10.1016/j.mtcomm.2024.108333.

References

[1] S.A. Wolf, D.D. Awschalom, R.A. Buhrman, J.M. Daughton, S. von Molnár, M. L. Roukes, A.Y. Chtchelkanova, D.M. Treger, Spintronics: a spin-based electronics vision for the future, Science 294 (2001) 1488–1495, https://doi.org/10.1126/science.1065389.

[2] S. Emori, P. Li, Ferrimagnetic insulators for spintronics: beyond garnets, J. Appl. Phys. 129 (2021) 020901, https://doi.org/10.1063/5.0033259.

[3] K. Uchida, S. Takahashi, K. Harii, J. Ieda, W. Koshibae, K. Ando, S. Maekawa, E. Saitoh, Observation of the spin Seebeck effect, Nature 455 (2008) 778–781, https://doi.org/10.1038/nature07321.

[4] P. Jiménez-Cavero, I. Lucas, A. Anadón, R. Ramos, T. Niizeki, M.H. Aguirre, P. A. Algarabel, K. Uchida, M.R. Ibarra, E. Saitoh, L. Morellón, Spin Seebeck effect in insulating epitaxial $\gamma-Fe_2O_3$ thin films, APL Mater. 5 (2017) 026103, https://doi.org/10.1063/1.4975618.

[5] L.J. Riddiford, J.J. Wisser, S. Emori, P. Li, D. Roy, E. Cogulu, O. Van, 'T. Erve, Y. Deng, S.X. Wang, B.T. Jonker, A.D. Kent, Y. Suzuki, Efficient spin current generation in low-damping Mg(Al, Fe)$_2$O$_4$ thin films, Appl. Phys. Lett. 115 (2019) 122401, https://doi.org/10.1063/1.5119726.

[6] M. Bohra, S. Prasad, N. Kumar, D.S. Misra, S.C. Sahoo, N. Venkataramani, R. Krishnan, Large room temperature magnetization in nanocrystalline zinc ferrite thin films, Appl. Phys. Lett. 88 (2006) 262506, https://doi.org/10.1063/1.2217253.

[7] M. Bohra, S. Prasad, N. Venkataramani, S.C. Sahoo, N. Kumar, R. Krishnan, Low temperature magnetization studies of nanocrystalline Zn-ferrite thin films, IEEE Trans. Magn. 49 (2013) 4249–4252, https://doi.org/10.1109/TMAG.2013.2239969.

[8] U. König, E.F. Bertaut, Y. Gros, M. Mitrikov, G. Chol, Models of the magnetic structure of zinc ferrite, Solid State Commun. 8 (1970) 759–764, https://doi.org/10.1016/0038-1098(70)90425-4.

[9] Y.F. Chen, D. Spoddig, M. Ziese, Epitaxial thin film $ZnFe_2O_4$: a semi-transparent magnetic semiconductor with high Curie temperature, J. Phys. D Appl. Phys. 41 (2008) 205004, https://doi.org/10.1088/0022-3727/41/20/205004.

[10] M. Bohra, R. Arras, J.-F. Bobo, V. Singh, N. Kumar, H. Chou, Multiple spintronic functionalities into single zinc-ferrous ferrite thin films, J. Alloy. Compd. 895 (2022) 162425, https://doi.org/10.1016/j.jallcom.2021.162425.

[11] M. Lorenz, M. Brandt, K. Mexner, K. Brachwitz, M. Ziese, P. Esquinazi, H. Hochmuth, M. Grundmann, Ferrimagnetic $ZnFe_2O_4$ thin films on SrTiO3 single crystals with highly tunable electrical conductivity, Phys. Status Solidi (RRL) Rapid Res. Lett. 5 (2011) 438–440, https://doi.org/10.1002/pssr.201105359.

[12] M. Bohra, S. Prasad, N. Venkataramani, N. Kumar, S.C. Sahoo, R. Krishnan, Narrow ferromagnetic resonance linewidth polycrystalline Zn-ferrite thin films, IEEE Trans. Magn. 47 (2011) 345–348, https://doi.org/10.1109/TMAG.2010.2081664.

[13] M. Desai, J. Dash, I. Samajdar, N. Venkataramani, S. Prasad, P. Kishan, N. Kumar, A TEM study on lithium zinc ferrite thin films and the microstructure correlation with the magnetic properties, J. Magn. Magn. Mater. 231 (2001) 108–112, https://doi.org/10.1016/S0304-8853(01)00036-1.

[14] G. Kresse, J. Hafner, Ab initio molecular-dynamics simulation of the liquid-metal–amorphous-semiconductor transition in germanium, Phys. Rev. B. 49 (1994) 14251–14269, https://doi.org/10.1103/PhysRevB.49.14251.

[15] G. Kresse, J. Furthmüller, Efficient iterative schemes for ab initio total-energy calculations using a plane-wave basis set, Phys. Rev. B. 54 (1996) 11169–11186, https://doi.org/10.1103/PhysRevB.54.11169.

[16] P.E. Blöchl, Projector augmented-wave method, Phys. Rev. B. 50 (1994) 17953–17979, https://doi.org/10.1103/PhysRevB.50.17953.

[17] J.P. Perdew, K. Burke, M. Ernzerhof, Generalized gradient approximation made simple, Phys. Rev. Lett. 77 (1996) 3865–3868, https://doi.org/10.1103/PhysRevLett.77.3865.

[18] S.L. Dudarev, G.A. Botton, S.Y. Savrasov, C.J. Humphreys, A.P. Sutton, Electron-energy-loss spectra and the structural stability of nickel oxide: an LSDA+U study, Phys. Rev. B. 57 (1998) 1505–1509, https://doi.org/10.1103/PhysRevB.57.1505.

[19] H.J. Monkhorst, J.D. Pack, Special points for Brillouin-zone integrations, Phys. Rev. B. 13 (1976) 5188–5192, https://doi.org/10.1103/PhysRevB.13.5188.

[20] K. Sharma, L. Calmels, D. Li, A. Barbier, R. Arras, Influence of the cation distribution, atomic substitution, and atomic vacancies on the physical properties of $CoFe_2O_4$ and $NiFe_2O_4$ spinel ferrites, Phys. Rev. Mater. 6 (2022) 124402, https://doi.org/10.1103/PhysRevMaterials.6.124402.

[21] A.I. Liechtenstein, M.I. Katsnelson, V.P. Antropov, V.A. Gubanov, Local spin density functional approach to the theory of exchange interactions in ferromagnetic metals and alloys, J. Magn. Magn. Mater. 67 (1987) 65–74, https://doi.org/10.1016/0304-8853(87)90721-9.

[22] S. Smidstrup, T. Markussen, P. Vancraeyveld, J. Wellendorff, J. Schneider, T. Gunst, B. Verstichel, D. Stradi, P.A. Khomyakov, U.G. Vej-Hansen, M.-E. Lee, S. T. Chill, F. Rasmussen, G. Penazzi, F. Corsetti, A. Ojanperä, K. Jensen, M.L. N. Palsgaard, U. Martinez, A. Blom, M. Brandbyge, K. Stokbro, QuantumATK: an integrated platform of electronic and atomic-scale modelling tools, J. Phys. Condens. Matter 32 (2019) 015901, https://doi.org/10.1088/1361-648X/ab4007.

[23] M.J. van Setten, M. Giantomassi, E. Bousquet, M.J. Verstraete, D.R. Hamann, X. Gonze, G.-M. Rignanese, The PseudoDojo: training and grading a 85 element optimized norm-conserving pseudopotential table, Comput. Phys. Commun. 226 (2018) 39–54, https://doi.org/10.1016/j.cpc.2018.01.012.

[24] M. Pajda, J. Kudrnovský, I. Turek, V. Drchal, P. Bruno, Ab initio calculations of exchange interactions, spin-wave stiffness constants, and Curie temperatures of Fe, Co, and Ni, Phys. Rev. B 64 (2001) 174402, https://doi.org/10.1103/PhysRevB.64.174402.

[25] Y. Li, Y. Li, X. Xu, C. Ding, N. Chen, H. Ding, A. Lu, Structural disorder controlled oxygen vacancy and photocatalytic activity of spinel-type minerals: a case study of $ZnFe_2O_4$, Chem. Geol. 504 (2019) 276–287, https://doi.org/10.1016/j.chemgeo.2018.11.022.

[26] M. Bohra, V. Singh, P. Grammatikopoulos, E. Toulkeridou, R.E. Diaz, J.-F. Bobo, M. Sowwan, Control of surface segregation in bimetallic NiCr nanoalloys immersed in Ag matrix, Sci. Rep. 6 (2016) 19153, https://doi.org/10.1038/srep19153.

[27] M. Bohra, P. Grammatikopoulos, V. Singh, J. Zhao, E. Toulkeridou, S. Steinhauer, J. Kioseoglou, J.-F. Bobo, K. Nordlund, F. Djurabekova, M. Sowwan, Tuning the onset of ferromagnetism in heterogeneous bimetallic nanoparticles by gas phase doping, Phys. Rev. Mater. 1 (2017) 066001, https://doi.org/10.1103/PhysRevMaterials.1.066001.

[28] Q. Tian, Q. Wang, Q. Xie, J. Li, Aqueous solution preparation, structure, and magnetic properties of nano-granular $Zn_xFe_{3-x}O_4$ ferrite films, Nanoscale Res. Lett. 5 (2010) 1518, https://doi.org/10.1007/s11671-010-9672-4.

[29] P.B. Allen, Effect of soft phonons on superconductivity: a re-evaluation and a positive case for Nb_3Sn, Solid State Commun. 14 (1974) 937–940, https://doi.org/10.1016/0038-1098(74)90397-4.

[30] S. Ayyappan, S.P. Raja, C. Venkateswaran, J. Philip, B. Raj, Room temperature ferromagnetism in vacuum annealed $ZnFe_2O_4$ nanoparticles, Appl. Phys. Lett. 96 (2010) 143106, https://doi.org/10.1063/1.3374332.

[31] A. Kumar, D.K. Pandya, S. Chaudhary, Electric field assisted sputtering of Fe_3O_4 thin films and reduction in anti-phase boundaries, J. Appl. Phys. 112 (2012) 073909, https://doi.org/10.1063/1.4757012.

[32] M. Bohra, D. Roy Chowdhury, J.-F. Bobo, V. Singh, Anomalous electric transport across Verwey transition in nanocrystalline Fe_3O_4 thin films, J. Appl. Phys. 125 (2019) 013901, https://doi.org/10.1063/1.5058150.

[33] J.G. Monsalve, C. Ostos, E. Ramos, J.G. Ramírez, O. Arnache, Insight into magnetic properties in zinc ferrite thin films by tuning oxygen content, Curr. Appl. Phys. 22 (2021) 77–83, https://doi.org/10.1016/j.cap.2020.12.015.

[34] S. Bera, A.A.M. Prince, S. Velmurugan, P.S. Raghavan, R. Gopalan, G. Panneerselvam, S.V. Narasimhan, Formation of zinc ferrite by solid-state reaction and its characterization by XRD and XPS, J. Mater. Sci. 36 (2001) 5379–5384, https://doi.org/10.1023/A:1012488422484.

[35] K.R. Sanchez-Lievanos, K.E. Knowles, Controlling cation distribution and morphology in colloidal zinc ferrite nanocrystals, Chem. Mater. 34 (2022) 7446–7459, https://doi.org/10.1021/acs.chemmater.2c01568.

[36] J. Wu, N. Li, J. Xu, Y. Jiang, Z.-G. Ye, Z. Xie, L. Zheng, Partially inverse spinel $ZnFe_2O_4$ with high saturation magnetization synthesized via a molten salt route, Appl. Phys. Lett. 99 (2011) 202505, https://doi.org/10.1063/1.3662840.

[37] R. Prabhu, B.N. Sahu, N. Venkataramani, S. Prasad, R. Krishnan, Anomalously large magnetic moment in nanocrystalline $Co_{0.3}Zn_{0.7}Fe_2O_4$ thin films, J. Phys. Commun. 1 (2017) 035010, https://doi.org/10.1088/2399-6528/aa8bf9.

[38] M.V. Nikolic, Z.Z. Vasiljevic, M.D. Lukovic, V.P. Pavlovic, J.B. Krstic, J. Vujancevic, N. Tadic, B. Vlahovic, V.B. Pavlovic, Investigation of $ZnFe_2O_4$ spinel ferrite nanocrystalline screen-printed thick films for application in humidity sensing, Int. J. Appl. Ceram. Technol. 16 (2019) 981–993, https://doi.org/10.1111/ijac.13190.

[39] S. Al Khabouri, S. Al Harthi, T. Maekawa, Y. Nagaoka, M.E. Elzain, A. Al Hinai, A. Al-Rawas, A. Gismelseed, A.A. Yousif, Composition, electronic and magnetic investigation of the encapsulated $ZnFe_2O_4$ nanoparticles in multiwall carbon nanotubes containing Ni residuals, Nanoscale Res. Lett. 10 (2015) 262, https://doi.org/10.1186/s11671-015-0971-7.

[40] H. Song, L. Zhu, Y. Li, Z. Lou, M. Xiao, Z. Ye, Preparation of $ZnFe_2O_4$ nanostructures and highly efficient visible-light-driven hydrogen generation with the assistance of nanoheterostructures, J. Mater. Chem. A. 3 (2015) 8353–8360, https://doi.org/10.1039/C5TA00737B.

[41] G. Yu, N. Peng, L. Zhou, Y. Liang, X. Zhou, B. Peng, L. Chai, Z. Yang, Selective reduction process of zinc ferrite and its application in treatment of zinc leaching residues, Trans. Nonferrous Met. Soc. China 25 (2015) 2744–2752, https://doi.org/10.1016/S1003-6326(15)63899-7.

[42] J.J. Melo Quintero, C.E. Rodríguez Torres, L.A. Errico, Ab initio calculation of structural, electronic and magnetic properties and hyperfine parameters at the Fe sites of pristine $ZnFe_2O_4$, J. Alloy. Compd. 741 (2018) 746–755, https://doi.org/10.1016/j.jallcom.2018.01.217.

[43] C.E. Rodríguez Torres, G.A. Pasquevich, P.M. Zélis, F. Golmar, S.P. Heluani, S. K. Nayak, W.A. Adeagbo, W. Hergert, M. Hoffmann, A. Ernst, P. Esquinazi, S. J. Stewart, Oxygen-vacancy-induced local ferromagnetism as a driving mechanism in enhancing the magnetic response of ferrites, Phys. Rev. B 89 (2014) 104411, https://doi.org/10.1103/PhysRevB.89.104411.

[44] J. Melo Quintero, K.L. Salcedo Rodríguez, F.A. Gómez Albarracín, H.D. Rosales, P. Mendoza Zélis, S.J. Stewart, L.A. Errico, C. Rodríguez Torres, On the deviation from a Curie–Weiss behavior of the $ZnFe_2O_4$ susceptibility: a combined ab-initio and Monte-Carlo approach, Heliyon 5 (2019) e01170, https://doi.org/10.1016/j.heliyon.2019.e01170.

[45] J.J. Melo Quintero, K.L. Salcedo Rodríguez, C.E. Rodríguez Torres, L.A. Errico, Ab initio study of the role of defects on the magnetic response and the structural, electronic and hyperfine properties of $ZnFe_2O_4$, J. Alloy. Compd. 775 (2019) 1117–1128, https://doi.org/10.1016/j.jallcom.2018.10.082.

[46] J.B. Goodenough, Magnetism and the Chemical Bond, Interscience Publishers, 1963.

[47] W. Geertsma, D. Khomskii, Influence of side groups on 90° superexchange: a modification of the Goodenough-Kanamori-Anderson rules, Phys. Rev. B 54 (1996) 3011–3014, https://doi.org/10.1103/PhysRevB.54.3011.

[48] R. Arras, L. Calmels, B. Warot-Fonrose, Half-metallicity, magnetic moments, and gap states in oxygen-deficient magnetite for spintronic applications, Appl. Phys. Lett. 100 (2012) 032403, https://doi.org/10.1063/1.3678028.

[49] V. Alman, A. Annadi, C. Murapaka, J. Pradhan, A. Haldar, V. Singh, M. Bohra, Thickness-driven magnetic behavior in Ni–Cr nanocrystalline thin films: implications for spintronics and magnetic cooling, ACS Appl. Nano Mater. 6 (2023) 10394–10401, https://doi.org/10.1021/acsanm.3c01343.